Journal of Materials Chemistry A

Accepted Manuscript

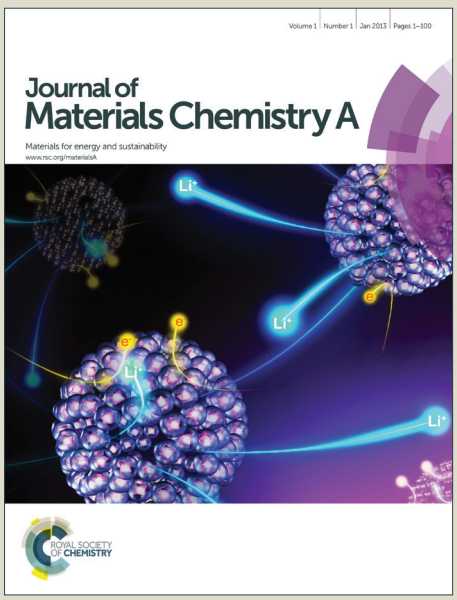

ROYAL SOCIETY OF CHEMISTRY

www.rsc.org/materialsA

Self-assembly of Si/ honeycomb reduced graphene oxide composite film as a binder-free and flexible anode for Li-ion batteries

Hong Tang, Jiang-ping Tu,* Xia-yuan Liu, Yi-jun Zhang, Sen Huang, Weng-zheng Li, Xiu-li Wang, and Chang-dong Gu

State Key Laboratory of Silicon Materials, Key Laboratory of Advanced Materials and Applications for Batteries of Zhejiang Provence, and Department of Materials Science and Engineering, Zhejiang University, Hangzhou 310027, China.

E−mail: tujp@zju.edu.cn; tujplab@zju.edu.cn

Tel: +86 571−87952856; Fax: +86 571−87952573

Abstract

A silicon/ honeycomb graphene composite film synthesized by "breath figure" method is developed as a high-performance anode material for lithium ion batteries. The honeycomb graphene structure can effectively prevent the agglomeration of the silicon nanoparticles, increase the electrical conductivity and reduce the transfer resistance of Li^+. The composite film presents high specific capacity and good cycling stability (1118 mAh g^{-1} at 50 mA g^{-1} up to 50 cycles), as well as enhanced rate capability. This approach to prepare such a honeycomb porous structure is low−cost and facile route for the silicon−based anode materials.

1. Introduction

Lithium ion batteries (LIBs) have been regarded as one of the most promising energy storage devices in electric vehicle applications for their high energy density, long cyclic life and environmental compatibility. [1–3] Recently, transition metal oxides, [4–8] tin alloys and oxides, [9,10] and silicon [11,12] had been extensively studied as anode materials for LIBs due to their high specific capacities. Of all, silicon has the highest theoretical specific capacity of 4200 mAh g^{-1} for $Li_{22}Si_5$, which is ten times higher than that of graphite (372 mAh g^{-1}). [13–16] Therefore, the silicon–based anode material has attracted considerable interest as a promising candidate for replacing the commercial carbonaceous materials.

Unfortunately, there are two primary problems of micron silicon needed to be addressed when used as an anode material: low intrinsic electrical conductivity and tremendous volume changes (> 300%) during the lithiation/delithiation process, leading to the collapse of the electrode structure and subsequent electrical disconnection from the current collector. [14,17–21] Thus, more and more fresh silicon surfaces exposed in the electrolyte to form the solid electrolyte interphase (SEI) layer. According to calculations,[22] the surface of silicon has the most stable position and the minimum Li–Si distances. The stress can also be effective relaxation so different nanostructured forms of silicon anodes with large specific surface area and peculiar surface structure have been achieved, for instance, nanoparticles, [23] nanotubes [24] and nanowires.[25] However, poor electrical conductivity of Si anodes still limits their applications. One effective strategy is to use electronically conductive agents or

coatings, such as different types of conductive carbon materials, [26–28] and highly conducting polymer, [29] which can not only improve the electrical conductivity, but also limit the huge volume change of silicon to keep the electrode integrity.

Graphene, a new class two-dimension material, with superior conductivity, large specific surface area and flexibility has been extensively used in designing of advanced Si–based anodes material [30,31] and other electrode materials such as Li_3VO_4[32] or VO_2 [33–35]. The reduced graphene oxide (rGO) can synergistically accommodate the volume change of encapsulated silicon particles, and maintain the structural and electrical integrity of the electrode. Besides, when the content of lithium ion is the maximum, the volume change of the silicon/graphene structure is smaller (24%) than the original silicon particles by the theoretical calculation.[36] Simple mechanical mixing processes usually lead to the agglomeration of silicon nanoparticles. [37] Therefore, self–assembly of silicon/graphene nanostructure is an effective route to avoid above problems.

In this present work, we develop a novel technique to fabricate Si/honeycomb rGO (Si/H–rGO) composite film by "breath figure" method. The Si/H–rGO composite film not only delivers a high reversible capacity but also presents a good high–rate capability. The improved cycling performance and highly reversible capacity are attributed to the novel three dimensional porous rGO architectures. The facile method provides a new approach for the Si-based anode materials for LIBs.

2. Experimental Section

Preparation of Si/H–rGO Composite Film

All reagents were analytical grade and used without further purification. GO was prepared from graphite powder according to the modified Hummers' method.[38] Briefly, 1 g of natural graphite powder was put into the solution of 45 mL of H_2SO_4 and 5 ml H_3PO_4 under stirring in a ice water bath, and then 0.75 g of $NaNO_3$ and 4.5 g of $KMnO_4$ were added sequentially. Successively, the mixture was stirred at 60 ℃ for 10 h, and further diluted at 95 ℃ for 1 h. Finally, 15 mL H_2O_2 (30%) was added into the mixture solution. The obtained product was filtrated and washed with diluted HCl aqueous solution (1/10 v/v) to remove the undissolved metal oxide and followed by washing with lots of distilled water to obtain the GO. Exfoliation of GO was achieved under ultrasonication for 2 h and dried by vacuum freeze drying.

The Si/H–rGO composite film was prepared according to the "breath figure" method reported before. [39–41] A certain amount of GO was exfoliated in distilled water to form a stable GO suspension with the concentration of 0.1 mg mL^{-1} by ultrasonic treatment. Then 2 mg of silicon particles (particle size: 20–50 nm) was added into the solution to form a GO/silicon suspension under punchy stirring. The pH value of top clean solution was adjusted close to 9 by 1 M KOH aqueous solution. Subsequently, chloroform solution containing 0.1 mg mL^{-1} dimethyldioctadecylammonium bromide (DODA·Br) was selected to titrate the GO water solution. Finally, the Si/GO/DODA complex was extracted the chloroform solution and the color of the solution changed to light brown. Typically, the honeycomb thin composite film was prepared by direct

casting 50 μL of Si/GO/DODA complex chloroform solution (0.1 mg mL^{-1}) onto the copper substrate under humid environment. When the film was totally dried, another 50 μL chloroform solution was added into the mixture. The composite films covering an area of *ca.* 15 mm^2 were left behind after the complete evaporation of the solvent and water. Subsequently, the honeycomb composite films were reduced at 90 ℃ for 16 h under the steam of hydrazine monohydrate. For comparison, the same method was used to prepare the honeycomb graphene film (H−rGO) (the loading is about 0.3−0.5 mg). The Si/rGO (the ratio of Si/rGO is also 1: 1) and rGO films without any porous structure were also prepared in dry environment.

Materials characterization

The microstructure and morphology of the products were characterized by X−ray diffraction (XRD, Rigaku D/max 2550 PC, Cu K_α), X−ray photoelectron spectroscopy (XPS, AXIS UTLTRADLD), scanning electron microscopy (SEM, Hitachi S−4700), and transmission electron microscopy (TEM, JEM 200CX at 160 kV, Tecnai G2 F30 at 300 kV). The Raman spectra were measured on a JobinYvon Labor Raman HR−800 using Ar−ion laser of 514.5 nm. Zetasizer3000HSA was used to test the Zeta potential for characterization of silicon, graphene and Si/H−rGO composite film.

Electrochemical measurements

The films were built on the copper foil and directly used as working electrode without any binder and carbon black. The electrochemical tests were performed using a coin−type half cell (CR 2025). Test cells were assembled in an argon−filled glove box

with the metallic lithium foil as both the reference and counter electrodes, 1 M $LiPF_6$ in ethylene carbonate (EC)−dimethyl carbonate (DME) (1: 1 in volume) as the electrolyte, and a polypropylene (PP) micro−porous film (Cellgard 2300) as the separator. The galvanostatic charge−discharge tests were conducted on a LAND battery program−control test system at different current densities between 0.01 and 1.5 V at room temperature (25 ± 1 ºC). Cyclic voltammetry (CV) tests were performed on a CHI660C electrochemical workstation in the potential range of 0− 3.0 V (vs. Li/Li^+) at a scanning rate of 0.1 mV s^{-1}. Electrochemical impedance spectroscopy (EIS) measurements were carried out in the frequency range from 100 kHz to 0.01 Hz under AC stimulus with 5 mV of amplitude.

3. Results and discussion

The formation of the honeycomb structure is based on the "breath figure" method. As demonstrated in Fig. 1a, the fabrication of the Si/H−rGO composite film involves following steps. First, DODA·Br is chosen to modify the surface of GO by the hydrophobic alkyl chains since GO is hydrophilic and the zeta potentials is −42 mV. The surfactant can also prevent the collapse and aggregation of adjacent graphene layers during the GO reduction process.[39,42] Second, the Si nanoparticles are negative charged (zeta potentials: −19 mV) from the thick silicon oxide (SiO_x).[37] When the silicon nanoparticles are dispersed in the GO/DODA complex (zeta potentials: 39 mV), well-mixed Si/GO/DODA nanocomposite can be obtained through electrostatic self-assembly. It can be clearly seen that the color of the GO aqueous solution

changes from dark brown to light yellow when adding DODA·Br and the color of the chloroform solution changes to dark brown (Fig. 1b). Finally, the Si/H−rGO composite film was obtained via organic solvent evaporation in the wet environment and then reduced by hydrazine monohydrate. The hydrazine vapor can combine with the oxygen-containing functional groups, which not only reduce the GO into graphene but also can impel graphene layer crosslink together by chemical bonding.[43,44] Fig. 2a shows a typical XRD pattern of the Si/H−rGO composite film. Obviously, the diffraction peaks of the composite film are matched well with the silicon crystal planes of (111), (220), (311), and an additional broad (002) diffraction peak at about 25 °. This confirms the conversion of GO to rGO after the hydrazine hydrate treatment as described in the previous literatures, [45,46] and the silicon particles are effective inserted into the H-rGO. Fig. 2b shows the Raman spectra of the composite film before and after exposure to N_2H_4 vapor. Two characteristic peaks are observed corresponding to the D and G bands of graphene based materials in the Raman spectra. I_D/I_G ratio is an important parameter to evaluate the graphitization degree of carbonaceous materials and the density of defects in graphene based materials. After N_2H_4 treatment, the I_D/I_G ratio increases from 0.9 to 1.03 and this result may be attributed to the presence of localized sp^3 defects within the sp^2 carbon network upon reduction of the exfoliated GO. [45,47]

Fig. 2c shows a low-magnification SEM image of the honeycomb structure of the Si/H−rGO composite film, which is formed on the copper substrate in moist atmosphere. The surface holes have a regular size of about 1.5 μm. It is easy to find

the small Si particles on the surface of H-rGO (Fig. 2d). TEM was further carried out to characterize the structure of the Si/H−rGO film. As shown in Fig. 2e, the Si nanoparticles are uniformly dispersed in the portholes of honeycomb structure (The mass ratio of silicon particles and rGO is 1: 1. The mass of active material on the Cu substrate is about 0.3−0.5 mg). More importantly, the honeycomb structure is beneficial to prevent the aggregation of Si nanoparticles during cycling and provide the space to release the volume expansion.

Fig. 3 shows the XPS spectra of the Si/H−rGO composite film. The detected elements are Si, C, O and Cu in the survey scan spectrum (Fig. 3a). As shown in Fig. 3b, the Si 2p XPS spectrum contains three components of Si−C at 99.9 eV, monatomic silicon at 99.0 eV and Si/SiO_x ($x < 2$) at 103.5 eV. There are no peaks at 110 and 105 eV, i.e., signals from SiO_2, [48] are absent in the composite film. The SiO_x species are possibly by the oxidation of freshly prepared Si nanocrystals with a high surface activity. In addition, the SiO_x thin layer plays an important role in intermediate phase interacting relatively strong with both Si and chemically derived graphene, which can enhance the adhesive force between Si and graphene. [48,49] The C 1s core level peak can be split into four components. The peaks of sp^2C−sp^2C, N−sp^2C and C=O of graphene sheets are detected at 284.6, 285.8, and 288.5 eV, respectively. The signal assigned to Si–C bond can be found in the C 1s spectrum at 284.3 eV. [50] Meanwhile, N 1s peak is also located at 400 eV (Fig. 3d), which is ascribed to a −C−N=N− type of N atom.[51,52] The above results demonstrate the covalent bonding of graphene to Si nanoparticles by means of DODA. It is generally believed that the covalent binding of

DODA to the graphene sheets is gotten through a single−electron transfer reaction mechanism according to the carbonaceous materials. [50,53]

Fig. 4a shows initial CV curves of Si/H−rGO composite film in the potential window of 0− 3 V (Li/Li^+) at a scan rate of 0.1 mV s^{-1}. It is clear that the CV curve of the first cycle is different from those of subsequent cycles. In the first cycle, the flat plateau becomes quite large below 0.1 V, which is related to the following conversion reaction: [54]

$$\text{Si (crystal)} \rightarrow \text{Li}_x\text{Si (amorphous)} \rightarrow \text{Li}_{15}\text{Si}_4 \text{ (crystal)} \leftrightarrow \text{Si (amorphous)}$$

The anodic part shows two peaks at 0.3 V and 0.5 V, corresponding to the dealloying of Li−Si alloys, which is consistent with previous reports. [17,30,53] The distinct reduction peaks at around 1.0 V− 1.5 V may be associated with the side reaction of Li^+ with the residual oxygen−containing groups of rGO−DODA, [47] as well as the formation of SEI layer on silicon particles.

Fig. 4b displays the initial discharge−charge profiles of the Si/H−rGO composite film at a current density of 50 mA g^{-1} between 0.01 V and 1.5 V. The initial discharge is 3559 mAh g^{-1} with a reversible charge capacity of 1686 mAh g^{-1} (the specific capacity is calculated according to the total mass). The irreversible capacity can be ascribed to the formation of SEI layer and the utilization of graphene, and the first coulombic efficiency is 47%. After the second cycle, the coulombic efficiency can stabilize, above 94% in the subsequent cycles. For comparison, the electrochemical performance of the Si/rGO, H−rGO and rGO was also investigated under the same electrochemical condition. Fig. 4c shows the cycling performances of Si/H−rGO,

Si/rGO, H–rGO and rGO films. After 50 cycles, the Si/H–rGO composite film delivers a reversible capacity of 1118 mAh g^{-1}, much higher than other electrodes (Si/rGO: 516 mAh g^{-1}; H-rGO: 381 mAh g^{-1}; and rGO: 212 mAh g^{-1}). Moreover, the rate capability of the Si/H–rGO composite film was also evaluated from 50 mA g^{-1} to 1000 mA g^{-1}. As shown in Fig. 4d, the Si/H–rGO composite film can deliver reversible capacities of about 1382, 1139, 925, 664, and 491 mAh g^{-1}, at a current density of 50, 100, 200, 500 and 1000 mA g^{-1}, respectively. And it has been proved that the cycling performance of pure silicon is very poor after 10 cycles. EIS measurements were employed to deeply understand the electrochemical performance of Si/H–rGO and Si particle electrodes. Fig. 5a shows the Nyquist plots of both the electrodes after 50 cycles from 100 kHz to 0.01 Hz in the fully charged state. They are composed of a depressed semicircle where a high-frequency semicircle and a medium-frequency semicircle overlap each other, and a long low-frequency line. Warburg impedance (Z_w) is related to the inclined line in the low-frequency region, which represents solid-state diffusion of Li^+ in the electrode materials. And R_{ct} is the charge-transfer resistance, which is indicated the semicircle in the middle, relating to charge transfer through the electrode/electrolyte interface. The intercept on the Z real axis in the high frequency region corresponds to the resistance of electrolyte (R_s).[30,55,56] The medium frequency range is related to the charge-transfer resistance occurring between active materials and liquid electrolyte. It clearly shows the R_{ct} of the Si/H–rGO composite film is much smaller than that of the pure Si particle electrode. The H-rGO plays an important role in making charge transfer much easily

at the electrode/electrolyte interface, and consequently decrease the internal resistance.[57,58] To check the morphology of the electrodes after cycling, the cells were disassembled after 50 cycles in the delithiated state. Fig. 5b shows the SEM image of the full delithiation Si/H−rGO composite film after 50 cycles. The Si/H−rGO electrode keeps the entirely honeycomb skeleton, which can not only effectively prevent the agglomeration of Si nanoparticles, but also release the stress of the volume expansion during lithiation/delithiation process.

Ultimately, the improved electrochemical performance of the Si/H−rGO composite film could be attributed to the following reasons. First, the honeycomb graphene structure provides plentiful pathways for efficient Li^+ diffusion/electron transport and promotes the fully infiltration of electrolyte. Second, the self−assembly composite film avoids the aggregation of Si nanoparticles and the flexible rGO supplies elastic buffer to accommodate the volume variation of Si during Li alloying and dealloying processes. Third, the composite electrode without polymeric binders can be excluded non-conducting components and reduce the transfer resistance of Li^+. [59−61]

4. Conclusions

A novel Si/honeycomb rGO composite film has been successfully prepared through self-assembly and “breath figure” method. As a flexible and binder-free electrode, the composite film displays good cyclic retention of 1118 mAh g^{-1} after 50 cycles and improved rate capability. The enhanced electrochemical performance can be attributed to the honeycomb rGO structure, which increases the electrical conductivity and

reduces the transfer resistance of Li^+ in the electrode. The synthesis approach presents a promising route for the anode material in advanced LIBs.

Acknowledgments

This work is supported by the National Science and Technology Support Program (2012BAC08B08), the Program for Innovative Research Team in University of Ministry of Education of China (IRT13037) and Key Science and Technology Innovation Team of Zhejiang Province (2010R50013).

References

1. X. Zhou, Y. X. Yin, L. J. Wan and Y. G. Guo, *Chem. Commun.*, 2012, **48**, 2198-2200.
2. S. Iwamura, H. Nishihara and T. Kyotani, *J. Power Sources*, 2013, **222**, 400-409.
3. C. L. Zhao, Q. Li, W. Wan, J. M. Li, J. J. Li, H. H. Zhou and D. S. Xu, *J.Mater. Chem.*, 2012, **22**, 12193-12197.
4. M. S. Wu and H. W. Chang, *J. Phys. Chem. C*, 2013, **117**, 2590-2599.
5. Q. Q. Xiong, J. P. Tu, X. H. Xia, X. Y. Zhao, C. D. Gu and X. L. Wang, *Nanoscale*, 2013, **5**, 7906-7912.
6. Y. J. Mai, X. H. Xia, R. Chen, C. D. Gu, X. L. Wang and J. P. Tu, *Electrochim. Acta*, 2012, **67**, 73-78.
7. L. Yu, Z. Y. Wang, L. Zhang, H. B. Wu and X. W. Lou, *J. Mater. Chem. A*, 2013, **1**, 122-127.
8. L. Zhang, H. B. Wu, S. Madhavi, H. H. Hng and X. W. Lou, *J. Am. Chem. Soc*., 2012, **134**, 17388-17391.
9. F. S. Ke, L. Huang, L. Jamison, L. J. Xue, G. Z. Wei, J. T. Li, X. D. Zhou and S. G. Sun, *Nano Energy*, 2013, **2**, 595-603.
10. C. D. Gu, H. Zhang, X. L. Wang and J. P. Tu, *Mater. Res. Bull.*, 2013, **48**, 4112-4117.
11. I. A. Profatilova, C. Stock, A. Schmitz, S. Passerini and M. Winter, *J. Power Sources*, 2013, **222**, 140-149.

12. Y. Y. Tang, X. H. Xia, Y. X. Yu, S. J. Shi, J. Chen, Y. Q. Zhang and J. P. Tu, *Electrochim. Acta*, 2013, **88**, 664-670.

13. H. Liu, L. Hu, Y. S. Meng and Q. Li, *Nanoscale*, 2013, **5**, 10376-10383.

14. E. L. Memarzadeh, W. P. Kalisvaart, A. Kohandehghan, B. Zahiri, C. M. B. Holt and D. Mitlin, *J. Mater. Chem.*, 2012, **22**, 6655-6668.

15. L. P. Zhang, X. P. Song, F. Wang, Q. Hu, Z. B. Sun, S. Yang, L. Q. Wang and S. D. Sun, *J. Solid State Electrochem.*, 2012, **16**, 2159-2167.

16. Y. Q. Zhang, X. H. Xia, X. L. Wang, Y. J. Mai, S. J. Shi, Y. Y. Tang, C. G. Cu and J. P. Tu, *J. Power Sources*, 2012, **213**, 106-111.

17. M. Zhou, T. W. Cai, F. Pu, H. Chen, Z. Wang, H. Y. Zhang and S. Y. Guan, *ACS Appl. Mater. Interfaces*, 2013, **5**, 3449-3455.

18. B. Wang, X. L. Li, X. F. Zhang, B. Luo, M. Jin, M. H. Liang, S. A. Dayeh, S. T. Picraux and L. J. Zhi, *ACS Nano*, 2013, **7**, 1437-1445.

19. X. D. Huang, K. Qian, J. Yang, J. Zhang, L. Li, C. Z. Yu and D. Y. Zhao, *Adv. Mater.*, 2012, **24**, 4419-4423.

20. Y. S. Park, J. Y. Kim and S. M. Lee, *Electrochem. Solid State Lett.*, 2011, **14**, A36-A38.

21. Y. Oumellal, N. Delpuech, D. Mazouzi, N. Dupré, J. Gaubicher, P. Moreau, P. Soudan, B. Lestriez and D. Guyomard, *J. Mater. Chem.*, 2011, **21**, 6201-6208.

22. V. V. Kulish, O. I. Malyi, M. F. Ng, P. Wu and Z. Chen, *RSC Adv.*, 2013, **3**, 4231-4236.

23. H. Wu, G. Zheng, N. A. Liu, T. J. Carney, Y. Yang and Y. Cui, *Nano Lett.*, 2012,

12, 904-909.

24. M. H. Park, M. G. Kim, J. Joo, K. Kim, J. Kim, S. Ahn, Y. Cui and J. Cho, *Nano Lett.*, 2009, **9**, 3844-3847.

25. C. K. Chan, H. Peng, G. Liu, K. McIlwrath, X. F. Zhang, R. A. Huggins and Y. Cui, *Nat. Nanotechnol.*, 2008, **3**, 31-35.

26. N. Dimov, S. Kugino and M. Yoshio, *Electrochim. Acta*, 2003, **48**, 1579-1587.

27. S. H. Ng, J. Wang, D. Wexler, K. Konstantinov, Z. P. Guo and H. K. Liu, *Angew. Chem. Int. Ed.*, 2006, **45**, 6896-6899.

28. L. F. Cui, Y. Yang, C. M. Hsu and Y. Cui, *Nano Lett.*, 2009, **9**, 3370-3374.

29. Z. P. Guo, J. Z. Wang, H. K. Liu and S. X. Dou, *J. Power Sources*, 2005, **146**, 448-451.

30. Y. Q. Zhang, X. H. Xia, X. L. Wang, Y. J. Mai, S. J. Shi, Y. Y. Tang, L. Li and J. P. Tu, *Electrochem. Commun.*, 2012, **23**, 17-20.

31. X. Zhou, A. M. Cao, L. J. Wan and Y. G. Guo, *Nano Res.*, 2012, **5**, 845-853.

32. Y. Shi, J. Z. Wang, S. L. Chou, D. Wexler, H. J. Li, K. Ozawa, H. K. Liu and Y. P. Wu, *Nano Lett.*, 2013, 13, 4715- 4720..

33. C. Nethravathi, B. Viswanath, J. Michael and M. Rajamath, *Carbon*, 2012, 50, 4839 – 4846.

34. C. Nethravathi, C. R. Rajamathi, M. Rajamathi, U. K. Gautam, X Wang, D. Golberg and Y. Bando, *ACS Appl. Mat. Interfaces,* 2013, 5, 2708−2714.

35. S. B. Yang, Y. J Gong, Z. Liu, L. Zhan, D. P. Hashim, L. L Ma, R. Vajtai, and P. M. Ajayan, *Nano Lett.*, 2013, 13, 1596−1601.

36. G. A. Tritsaris, E. Kaxiras, S. Meng and E. Wang, *Nano Lett.*, 2013, **13**, 2258-2263.

37. X. Zhou, Y. X. Yin, L. J. Wan and Y. G. Guo, *Adv. Energy Mater.*, 2012, **2**, 1086-1090.

38. W. S. Hummers and R. E. Offeman, *J. Am. Chem. Soc.*, 1958, **80**, 1339-1339.

39. S. Y. Yin, Y. Y. Zhang, J. H. Kong, C. J. Zou, C. M. Li, X. H. Lu, J. Ma, F. Y. C. Boey and X. D. Chen, *ACS Nano*, 2011, **5**, 3831-3838.

40. G. K. Wang, X. Sun, F. Y. Lu, H. T. Sun, M. P. Yu, W. L. Jiang, C. S. Liu and J. Lian, *Small*, 2012, **8**, 452-459.

41. L. W. Zhu, L. S. Wan, J. Jin and Z. K. Xu, *J. Phys. Chem. C*, 2013, **117**, 6185-6194.

42. M. Srinivasarao, D. Collings, A. Philips and S. Patel, *Science*, 2001, **292**, 79-83.

43. Z. Q. Niu, J. Chen, H. H. Hng, J. Ma and X. D. Chen, *Adv. Mater.* 2012, 24, 4144-4150.

44. L. L. Jiang and Z. J. Fan, *Nanoscale,* 2014, DOI: 10.1039/c3nr04555b.

45. Y. Liu, Y. L. Ying, Y. Y. Mao, L. Gu, Y. W. Wang and X. S. Peng, *Nanoscale*, 2013, **5**, 9134-9140.

46. Y. Lu, X. L. Wang, Y. J. Mai, J. Y. Xiang, H. Zhang, L. Li, C. D. Gu, J. P. Tu and S. M. Mao, *J. Phys. Chem. C*, 2012, **116**, 22217-22225

47. F. Tuinstra and J. L. Koenig, *J. Chem. Phys.*, 1970, **53**, 1126-1130.

48. X. Xin, X. F. Zhou, F. Wang, X. Y. Yao, X. X. Xu, Y. M. Zhu and Z. P. Liu, *J.*

Mater. Chem., 2012, **22**, 7724-7730.

49. J. Kaspar, M. Graczyk Zajac and R. Riedel, *Solid State Ionics*, 2012, **225**, 527-531.

50. S. N. Yang, G. R. Li, Q. Zhu and Q. M. Pan, *J. Mater. Chem.*, 2012, **22**, 3420-3425.

51. C. Martin, O. Crosnier, R. Retoux, D. Bélanger, D. M. Schleich and T. Brousse, *Adv. Funct. Mater.*, 2011, **21**, 3524-3530.

52. C. Martin, M. Alias, F. Christien, O. Crosnier, D. Bélanger and T. Brousse, *Adv. Mater.*, 2009, **21**, 4735-4741.

53. A. Ricci, C. Bonazzola and E. J. Calvo, *Phys. Chem. Chem. Phys.*, 2006, **8**, 4297-4299.

54. Z. Y. Lu, J. X. Zhu, D. Sim, W. H. Shi, Y. Y. Tay, J. Ma, H. H. Hng and Q. Y. Yan, *Electrochim. Acta*, 2012, **74**, 176-181.

55. Y. Zhang, M. Xu, F. Wang, X. P. Song, Y. H. Wang and S. Yang, *J. Phys. Chem. C*, 2013, **117**, 12346-12351.

56. M. M. Rahman, J. Z. Wang, M. F. Hassan, D. Wexler and H. K. Liu, *Adv. Energy Mater.*, 2011, **1**, 212-220.

57. C. H. Lim, A. G. Kannan, H. W. Lee and D. K. Kim, *J. Mater. Chem. A*, 2013, **1**, 6183-6190.

58. Q. Q. Xiong, J. P. Tu, Y. Lu, J. Chen, Y. X. Yu, X. L. Wang and C. D. Gu, *J Mater. Chem.*, 2012, **22**, 18639-18645.

59. B. Wang, X. L. Li, B. Luo, Y. Y. Jia, L. J. Zhi, *Nanoscale*, 2013, **5**, 1470-1474.

60. J. X. Zhu, D. Yang, X. H. Rui, D. Sim, H. Yu, H. E. Hoster, P. M. Ajayan, Q. Y. Yan, *Small*, 2013, **9**, 3390-3397.

61. G. Jo, I. Choi, H. Ahn, M. J. Park, *Chem. Commum.*, 2012, **48**, 3987-3989

Figure captions

Fig. 1 Formation processes of Si/H−rGO composite film: (a) schematic drawing of the preparation of the Si/H−rGO composite film based on GO; (b) photographs of the GO solution during phase transfer process by DODA.

Fig. 2 (a) XRD pattern of Si/H−rGO composite film. (b) Raman spectra of the Si/H−GO and Si/H−rGO composite films; (c, d) SEM images of Si/H−rGO composite film; (e f) TEM images of Si/H−rGO composite film.

Fig. 3 XPS spectra of Si/H−rGO composite film: (a) survey scan; (b) Si 2p; (c) C 1s; (d) N 1s.

Fig. 4 (a) CV curves of Si/H−rGO composite film in the initial four cycles at a scan rate of 0.1 mV s^{-1} in the potential range of 0 to 3.0 V (Li/Li^+), (b) galvanostatic discharge/charge profiles in the initial four cycles at a current density 50 mA g^{-1}, (c) cycling performance of Si/H−rGO, Si/rGO, H−rGO and rGO films at a current density of 50 mA g^{-1}, (d) Rate capability of Si/H−rGO composite film and pure silicon at various current densities ranging from 50 to 1000 mA g^{-1}.

Fig. 5 (a) Nyquist plots of Si/H−rGO and Si particle electrodes after 50 cycles from 100 kHz to 0.01 Hz in the fully charged state, (b) a SEM image of the full delithiation Si/H−rGO composite film electrode after 50 cycles.

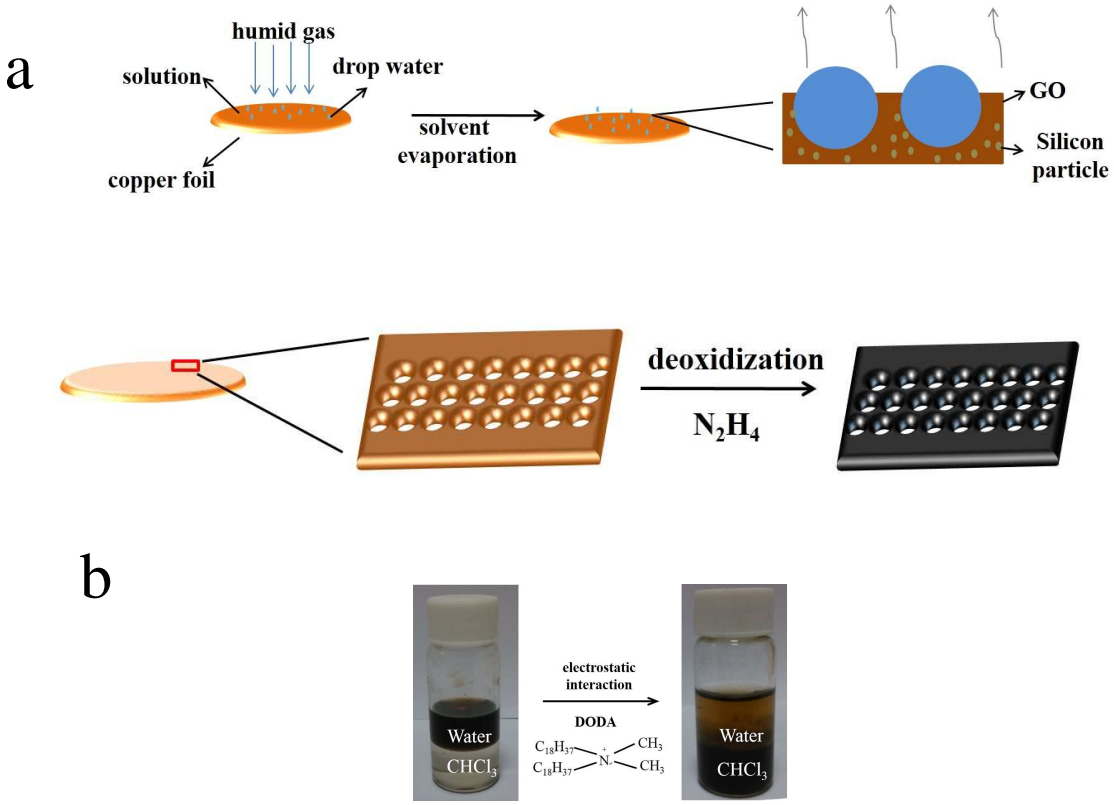

Fig. 1

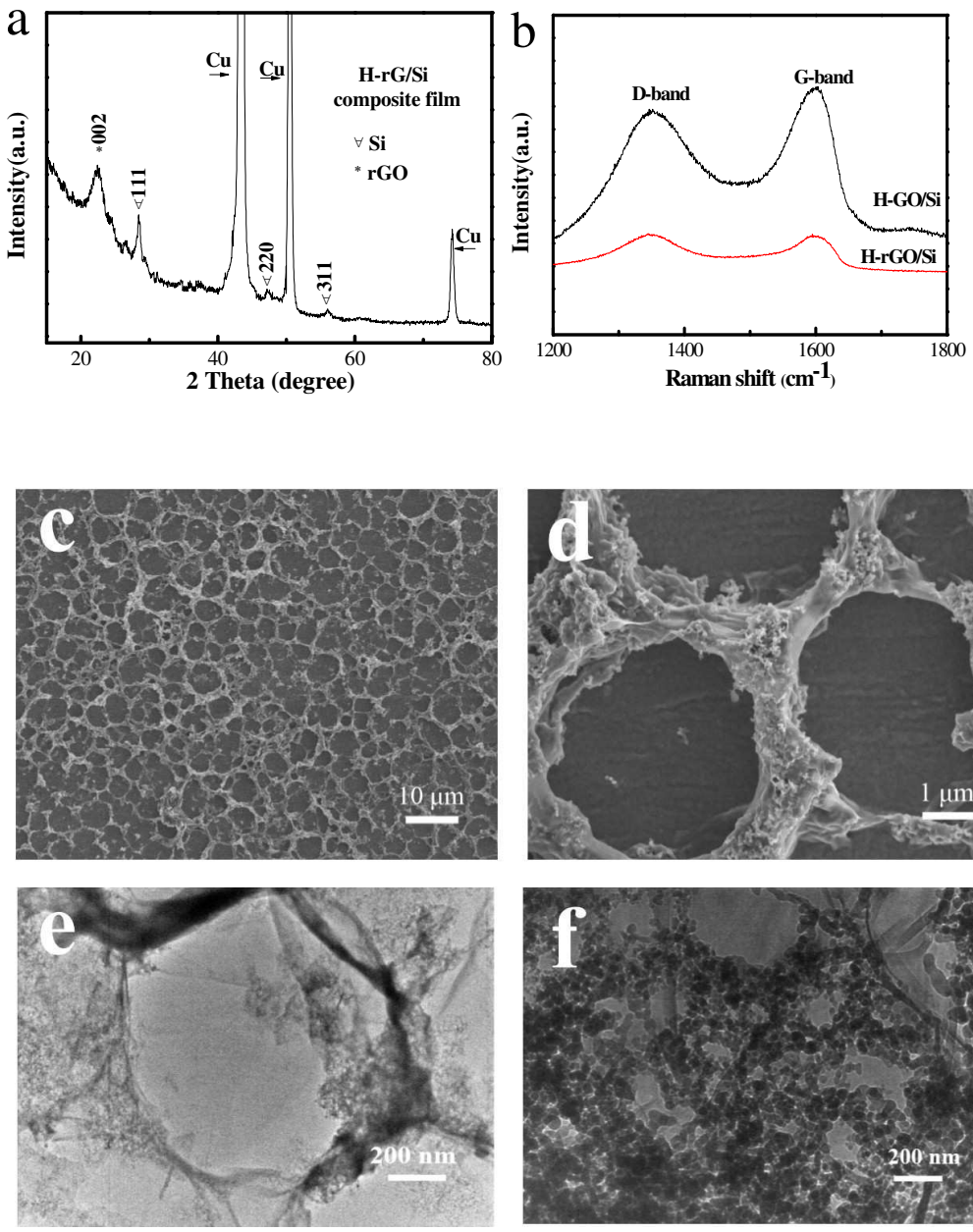

Fig. 2

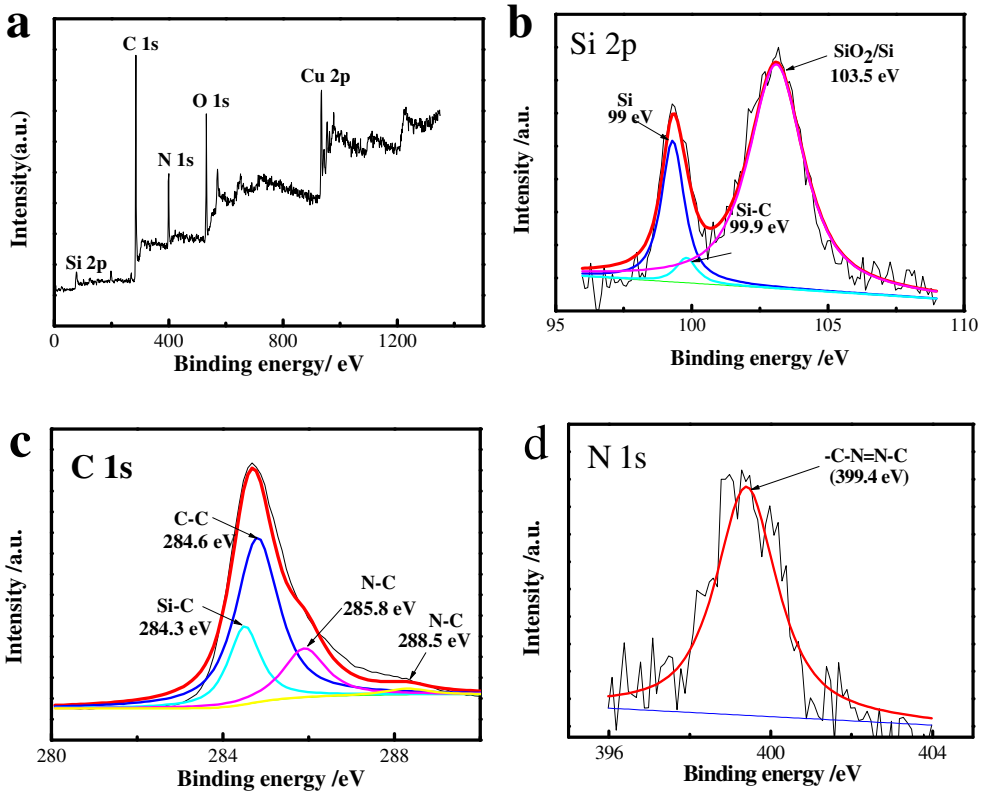

Fig. 3

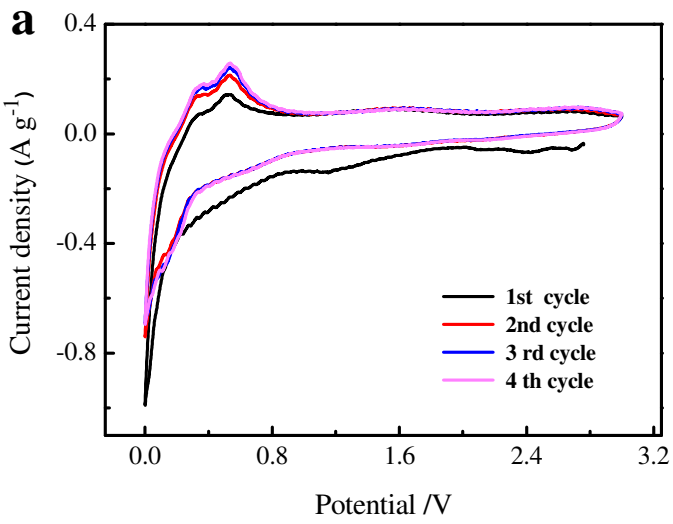

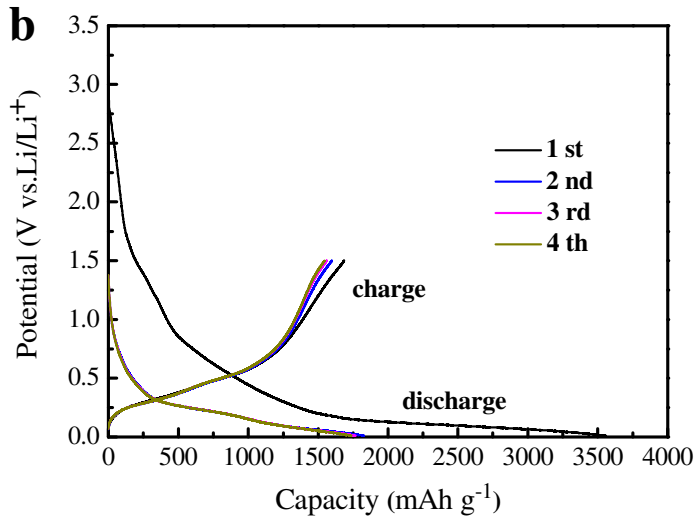

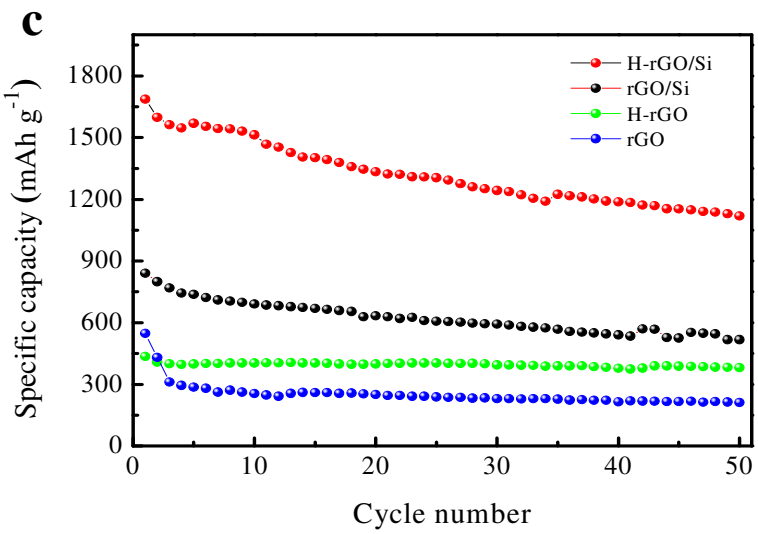

Fig. 4

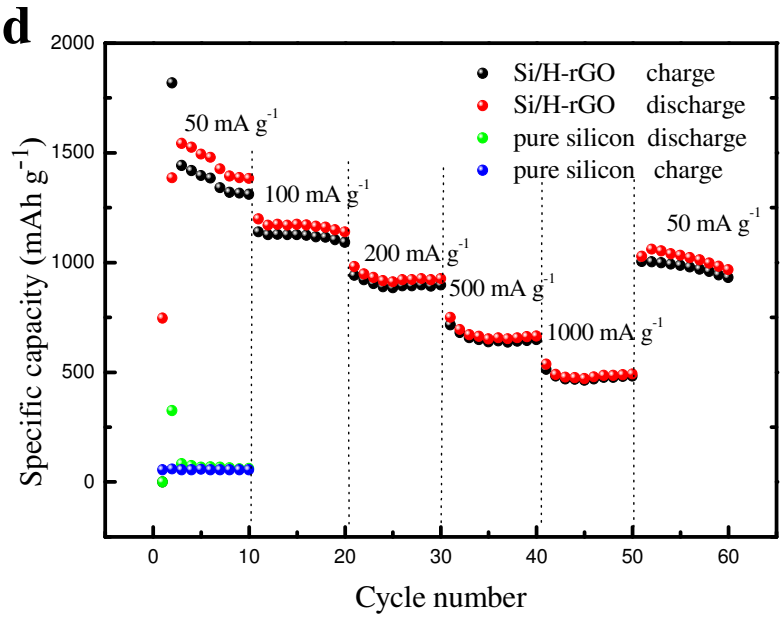

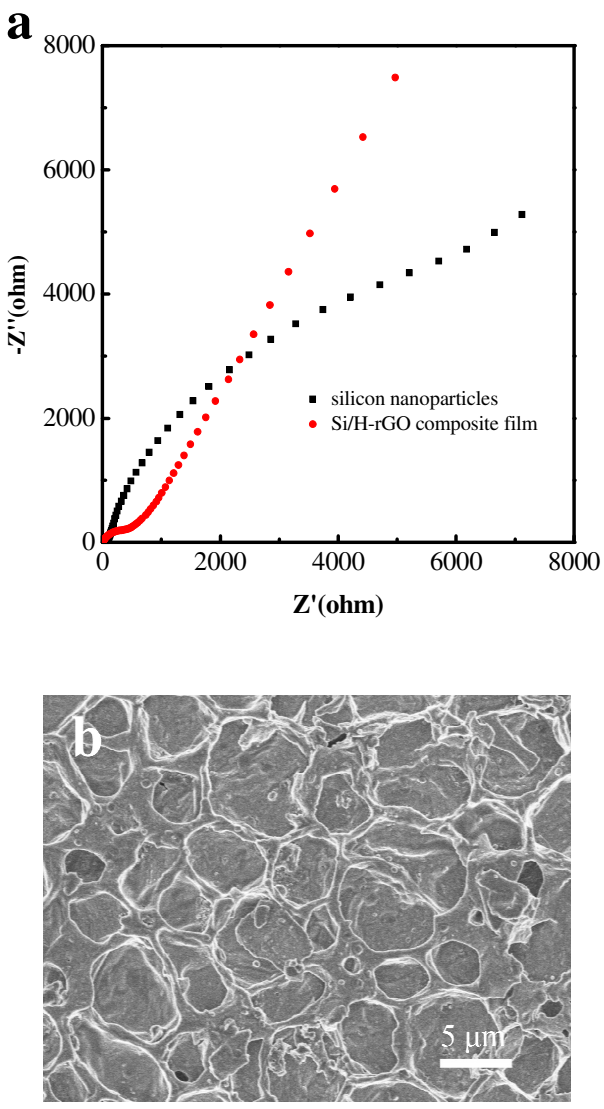

Fig. 5